Miniaturized omnidirectional flexible side-view endoscope for rapid monitoring of thin tubular biostructures

BJORN PAULSON,[1,2] **SANGHWA LEE,**[1,2] **YOUNGKYU KIM,**[1,2] **YOUNGJIN MOON,**[1,2] **AND JUN KI KIM**[1,2,3]

[1]*Biomedical Engineering Research Center, Asan Institute for Life Sciences, Asan Medical Center, 88, Olympic-ro 43-gil, Seoul, 05505, South Korea*
[2]*Department of Convergence Medicine, University of Ulsan, College of Medicine, 88, Olympic-ro 43-gil, Seoul, 05505, South Korea*
[3]*kim@amc.seoul.kr*

Abstract: Endoscopic imaging allows longitudinal observation of epithelial pathologies in tubular organs throughout the body. However, the imaging and optical diagnosis of tubular biostructures such as small animal models and small pediatric organs require appropriately miniaturized devices. A miniaturized catadioptric flexible side-view endoscope is proposed with omnidirectional field of view (FOV) in the transverse direction and sub-mm-scale feature resolution. The FOV in the longitudinal direction is 50°. Images are unwrapped and stitched together to form composite images of the target by two different algorithms, revealing a composite FOV of more than 3.5 cm × 360°. The endoscope is well suited for minimally invasive rapid monitoring of thin tubular organs in pediatric patients, as well as for imaging of small animal disease models at near-cellular resolution.

1. Introduction

Catadioptric devices, consisting of a combination of reflective and refractive elements, are uniquely suited for applications requiring instantaneous imaging of a panoramic field of view with a single sensor, and as a result they have found applications in fields as diverse as computer vision and navigation [1], industrial oil pipe inspection [2], and wide-angle surveillance [3,4], as well as in gastrointestinal imaging [5–7]. More recently, several teams have investigated side-viewing but non-catadioptric endoscopes for biological applications, such as esophageal endoscopy [8], and brain imaging [9,10].

In the biological sciences, as in industry, there is high demand for miniaturized imaging technology. A large community of researchers is involved in the development of small animal models of cancer in tubular epithelia such as the oral cavity [11], esophagus [12,13], and the colon [14–18]. There is also significant interest in micro-endoscopic imaging of the cardiac organs and the brain [19,20]. Small animal models allow quick and precise tailoring of genetic variants to reveal chemical signaling pathways, reduce the time and cost of experiments, and allow preclinical evaluation of potential therapeutic compounds [21]. Transfection of fluorescence-inducing viral vectors has allowed the fluorescent tagging of tumor cells for orthotopic injection into the colon wall [14–18]. Fluorescent pharmaceutical compounds have also been under development [22]. For the imaging of these targets *in vivo* and the full longitudinal monitoring of the tumor development cycle, miniaturized side-view endoscopes are necessary. Miniaturized endoscopes developed for small-animal applications may later be adapted for pediatric and minimally-invasive clinical applications.

Catadioptric endoscope probes allow side-view imaging behind epithelial folds, which are not accessible to surgeons when standard or wide-angle endoscopes are used [23,24], potentially enabling the rapid detection of early-formation lesions. At present, state-of-the-art side-view imaging is performed by rotating a mirrored micro-endoscope probe to stitch

together cylindrical panoramic composite images [9,25]. However, the movement of the imaging target due to autonomous tissue motion and experimental limitations results in distorted or failed stitching, reducing the effective size of images. Furthermore, the rotation of endoscope probes increases experimental invasiveness, resulting in failures of image stitching, and tissue damage.

By imaging a panoramic region with a single sensor, catadioptric probes provide potential solutions to these issues. Indeed, several research groups have developed side-view colonoscope prototypes for clinical use in human gastroenterology, and these probes achieve video images in viewing the large intestine [5,26,27]. Catadioptric probes with a panoramic field of view would allow the simultaneous capture of panoramic views deep into folded tissues without the need to correct for tissue motion. Several "dual view" and "reverse view" catadioptric endoscope probes have been either proposed or demonstrated recently. Of these, the smallest device diameter reported so far was in a cone-based capsule endoscope of diameter 8 mm [28]. However, cone-based capsule endoscopes suffer from significant astigmatism and field curvature aberrations [29].

In this paper, we demonstrate a family of novel flexible miniaturized micro-endoscopes based on a single-fold catadioptric mirror design, which give a 360° side-view image of the intestinal wall. The mirrors are demonstrated in parabolic geometry, and are fabricated by 3D printing, while a number of off-the-shelf miniaturized lens assemblies are compared. Composite image formation by stitching together a number of sequential full-diameter images is demonstrated, and the modulation transfer function (MTF) is measured by the edge target method. The probe is applied for imaging of the interior of a pediatric cardiac phantom fabricated by 3D printing, resulting in the first realistic phantom image captured by a miniaturized catadioptric probe, to the best knowledge of the authors.
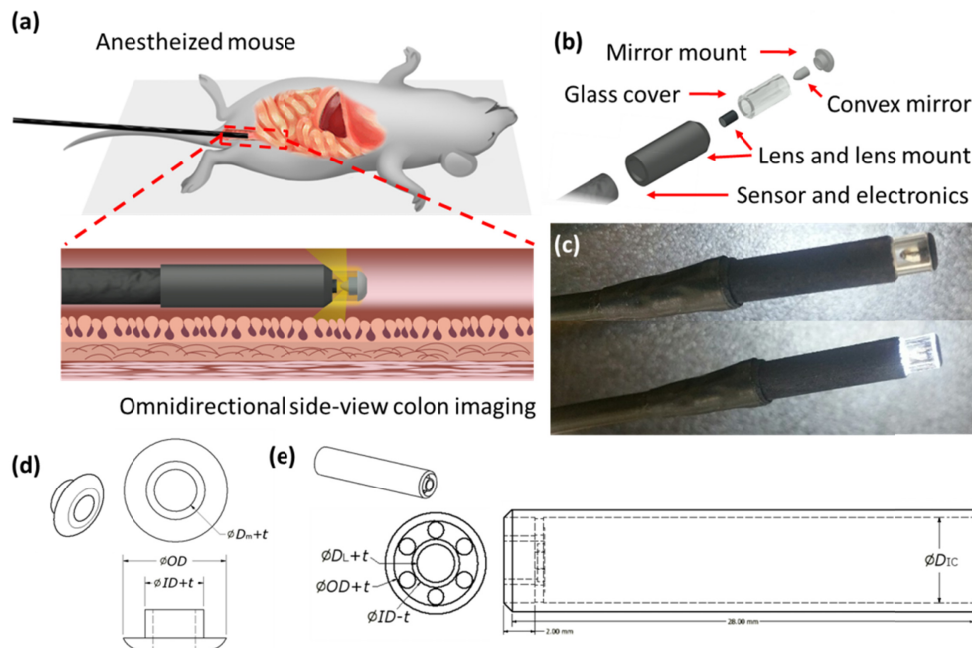

Fig. 1. Conception and realization of the miniaturized catadioptric device. (a) Example usage of a proposed flexible catadioptric micro-endoscope. The goal of the catadioptric device is to enable panoramic imaging into the thin tubular structures of the small animal and pediatric epithelial tissues. (b) The simple device consists of six parts and (c) as realized, allows imaging as well as illumination. (d) Scale design of a representative mirror mount and (e) lens mount for additive manufacturing.

2. Device design and experimental setup

In the application to side-view biological imaging (Fig. 1(a)), epithelial tissues such as the colon, esophagus, trachea and even cerebral and vascular tissues will surround an endoscopic probe such that the side-view probe is located at the central position of the tubular organs [6,29–31], thereby maintaining a known working distance. To miniaturize the probe and thereby minimize tissue damage, it was decided to focus on a single-fold catadioptric geometry. In this way, not only could the probe be miniaturized, but aberrations introduced by the mirror processing could be minimized, and the mirror assembly could be designed without an additional interior aperture.

The standard optical model for catadioptric devices is the single-view-point design [30], which results in an undistorted mapping between the world frame and the camera image, provided that mirror geometries are selected from the conic sections [32]. Compared to other strategies, mapping the catadioptric device field of view to a cylindrical projection of the world frame, trades a loss of overall image pixels and resolution for a wider field of view and simultaneous imaging in multiple directions [5]. For miniaturized catadioptric devices, where sensor area is at a premium (the commercially available sensors used in this study had a sensor width of 1.2 mm on a 3 mm wide package), device resolution is primarily limited by the field of view (FOV) of the lens. The first goal of lens selection or design is thus to maximize the image of the mirror in the sensor FOV at the design working distance. Careful mirror selection will then minimize the area of the image sensor which captures the reflection of the sensor itself in the mirror.

Three narrow-diameter, commercially available lenses were identified which met the required specifications of low aberration, a diameter of less than 3 mm, and a working distance of less than 5 mm. These were the SELFOC gradient index microlens, and the Sumita SEL 110 and the Sumita SEL 120 miniaturized lens assemblies.

The mirror was designed to minimize the field of view which reflected the lens, and for this purpose a parabolic geometry was found to be superior to spherical or hyperbolic geometries. The mirrors shown in Table 1 were fabricated of unprotected aluminum, and image quality was determined qualitatively, based on direct comparison of resolved features from identical printed cylindrical targets, as shown in Fig. 2. Conical mirror geometries show high astigmatism, due to their previously observed large birefringence and high field distortion [29]. For spherical and parabolic mirrors, a lower radius of curvature results in higher-resolution images, but also reduces the field of view. Best image quality was achieved by pairing a SEL 120 lens assembly (Sumita, Japan) with a parabolic mirror of focus 0.172 mm and diameter 2 mm (Table 1 and Fig. 2).

Mirrors were fabricated of unprotected aluminum by an ultraprecise machining process (K-Bio Health, Osong, Korea). Tolerances for mirror manufacture were ± 0.003 mm.

Lens and mirror mounts which were fabricated by additive manufacturing were used to immobilize lenses and mirrors relative to a transparent quartz tube of fixed length, as well as relative to the image sensor, as shown in Fig. 1(b). Representative mirror mount and lens mount schematics are shown in Fig. 1(d) and 1(e), respectively. Mirror mounts had diameter matching that of the quartz or acryl tube to be used (OD = 5.00 mm), with an extrusion which fit snugly within the tube (ID = 3.00 mm) and around the mirror (D_m in Table 1), with tolerances of t = 0.10 mm. Lens mounts (length 28.00 mm) contained a hollow chamber for the sensor and integrated circuit (D_{IC} = 5.00 mm), a hole which fit snugly around the lens assembly (D_L = 1.00 mm for SELFOC, 1.2 mm for SEL110, and 2.2 mm for SEL120), and extrusions to fit snugly around and within the tube (OD and ID, respectively). Six additional holes of radius 0.5 mm allowed for the draining of fluids during manufacture. Lens mounts were fabricated on a Formlabs Form2 stereolithographic (SLA) printer using white photopolymer resin (FLGPWH03) and grey resin (RS-F2-PRGR-01), followed by an isopropyl alcohol rinse to achieve a print resolution of 0.05 × 0.05 × 0.025 mm. Mirror mounts were fabricated on a ProJet 3500 SD printer using translucent VisiJet M3 Crystal

resin at 375 × 375 × 790 DPI resolution with 32 micron layers. Tolerances for mirror and lens mounts in the axial direction were thus 0.032 and 0.025 mm, respectively. Parts printed on the ProJet were cleaned by heating at 65 °C to remove paraffin support structures, followed by rinsing in an oil-filled ultrasonic bath at 65 °C to remove residue. Image sensors of 1/9" standard were used as integrated (Etron Technology, Inc., Taiwan), and consisted of a model GC0309 sensor (Galaxycore Technology Inc., China) with 480 × 640 resolution at 30 fps VGA (Table 2). When applicable, a quartz or acryl tube was ground to length (± 0.1 mm) on sandpaper, and the parts were assembled by hand.
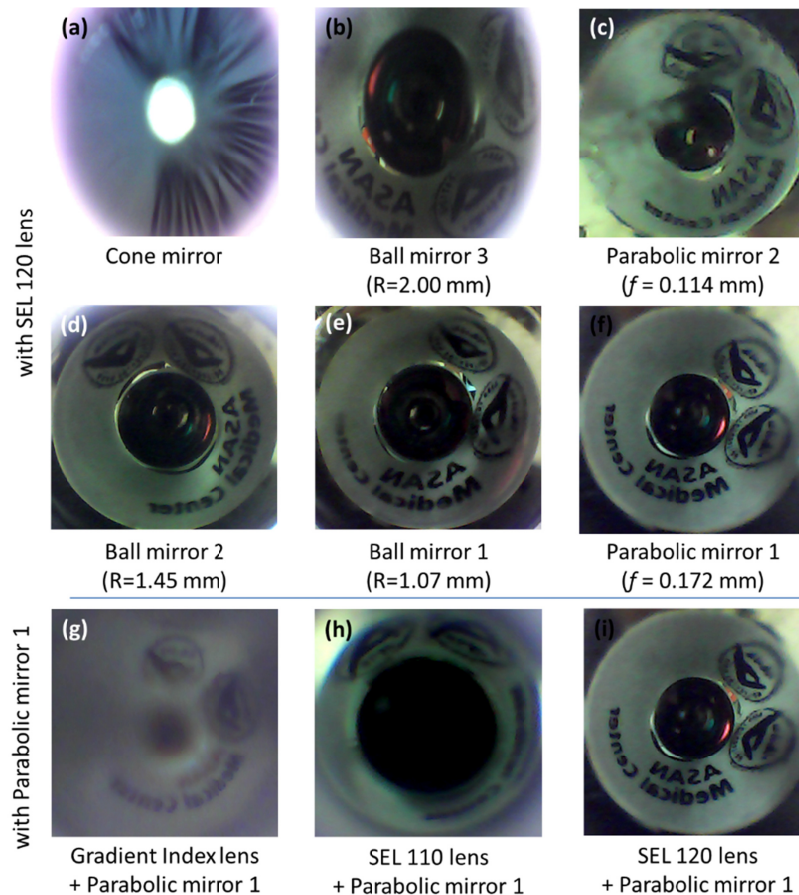

Fig. 2. Comparison of best focus image quality (a-e) for the catadioptric mirrors of Table 1, show that best combination of focus, resolution, and field of view are obtained (a-f) with Parabolic Mirror 1, a parabola of diameter 2.00 mm and focus 0.172 mm, and (g-i) the SEL 120 lens assembly. Note that (f) and (i) are intentionally identical.

Final devices were completed by immobilization with NOA 81 UV-curing polymer (Norland Products Inc., USA). The mirrors and sensors were immobilized with respect to the mirror and lens mounts, respectively, and the lenses were fixed into their mounts flush to the image sensors. The mirror mount was then inserted into the end of the quartz tube, and the tube was fit snugly into the corresponding groove in the lens mount. After verifying the alignment and focus of the mirror assembly with respect to the sensor assembly, the joints between assemblies were filled with NOA 81 and cured using a high-power UV LED (ThorLabs, USA).

The final devices had dimensions suitable for human and animal colonoscopy. The optical portion defined by the 1.5-mm-thick quartz tube has a diameter of 5 mm and a length of 7

mm, making the device suitable for small animal colonoscopy. The rigid distal portion has a length of 32 mm and a diameter of 5.25 mm, making the device comparable in dimensions to existing colonoscopy probes [33]. With thinner packaging and smaller image sensors, diameters as low as 3.5 mm will be accessible. The proximal flexible length of the device was about 2 m, which is also a suitable length for colonoscopes in the clinic.

Figure 3 shows the optical layout of the device, including a parabolic mirror. The device was simulated in Zemax with three paraxial lenses standing in for the SEL 120 lens assembly (Fig. 3(a)), to obtain the theoretical performance limitations of the design. Nine field components demonstrate device performance to vary significantly over an object plane FOV of 4.45 mm (about 65°). Ray tracing was used to calculate spot sizes, which show astigmatism/birefringence and varied with angle as shown in Fig. 3(b), with a minimum spot size of 0.025 microns for a chief ray at +10° (object coordinate +0.103 mm from the perpendicular), and a maximum spot size of 20 microns for a chief ray at −20° (−1.002 mm object). The ray at +57° (+3.458 mm object) showed a spot size of 2.54 microns, indicating that resolution is optimal at a viewing inclination near 10° to the perpendicular.

The modulation transfer function was estimated to vary highly based on measurement position (Fig. 3(c)), and a simulated grid image shows the expected cylindrical projection onto the image sensor (Fig. 3(d)).
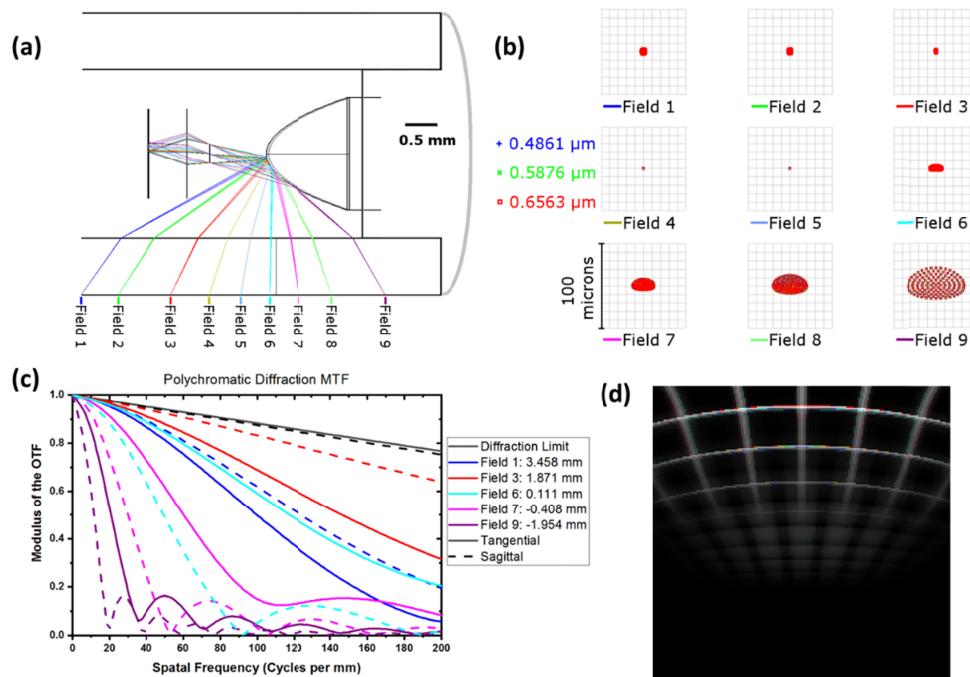

Fig. 3. Optical properties of the panoramic endoscope as-designed (a) Optical schematic of the device. (b) Spot sizes of the fields from +57° to −30°. (c) Calculated MTF of the device in selected fields. Measurements in mm denote object position axially from the mirror perpendicular. (d) Simulated cylindrical projection onto the image sensor.

The experimental modulation transfer function was measured by the slanted edge method. Cylindrical slanted edge targets with 60° and 45° angles were fabricated with resolution up to 1000 dpi (38 lp/mm) by printing a target pattern on standard (50 g) paper and wrapping around cylindrical molds. Targets were imaged individually under identical conditions, and MTF was calculated using Mitja's MTF plugin for ImageJ [34].

Table 1. Specifications of the mirrors

Parameters	Cone mirror	Ball mirror 1	Ball mirror 2	Ball mirror 3	Parabolic mirror 1	Parabolic mirror 2
Material	Protected Aluminum	Unprotected Aluminum				
Diameter D_m (mm)	2.00	1.07	1.45	2.00	2.00	2.00
Height (mm)	1.00	0.535	0.725	1.00	1.45	2.20
Focus or radius (mm)	n/a	0.535	0.725	1.00	0.172	0.114

Table 2. Specifications of the chip sensor

Parameters	Specifications
Supply Voltage	2.8 V
Chip size	2.64 mm × 2.22 mm x 0.69 mm
Pixel size	2.5 µm × 2.5 µm
Bit rate	24 MHz
Resolution	640 × 480

3. Results and discussion

For the clinical application of catadioptric imagers, it is desirable to create cylindrical projections of the initial images and to composite those images together into cylindrical composites of the target tubular biosystem. Figure 4 shows a demonstration of two different versions of this unwrapping algorithm and image composition process. As the probe is moved down a cylindrical surface, images are captured, as shown schematically in Fig. 4(a). In the first process, these images are unwrapped to a cylinder individually using a polar coordinate transformation. The unwrapped images are then composited to obtain a larger image using a panorama stitching algorithm [35]. Figure 4(b) shows the unwrapped grid template images, while in Fig. 4(c), the grids are combined into a composite image. This technique is advantageous when the movement of the probe is not smooth, but it is limited by the requirement that features for stitching be comparable between images.

A second method for image unwrapping allows for the automatic retrieval of a cylindrical image from video. A single line of the composite image is interpolated from a circular region of each frame of an endoscopy video, giving a very quick and feature-independent unwrapped cylinder. Figure 4(d) shows this counterclockwise interpolation along a circular region in each frame to give a composite unwrapped cylindrical image (Fig. 4(e)).

Several distortions observed in actual images show difficulties which are not encountered in simulated images, namely that the aspect ratio of features in the image depends on the distance from the feature to the mirror. This can result in distortion when using non-radial (or improperly centered) imaging targets.
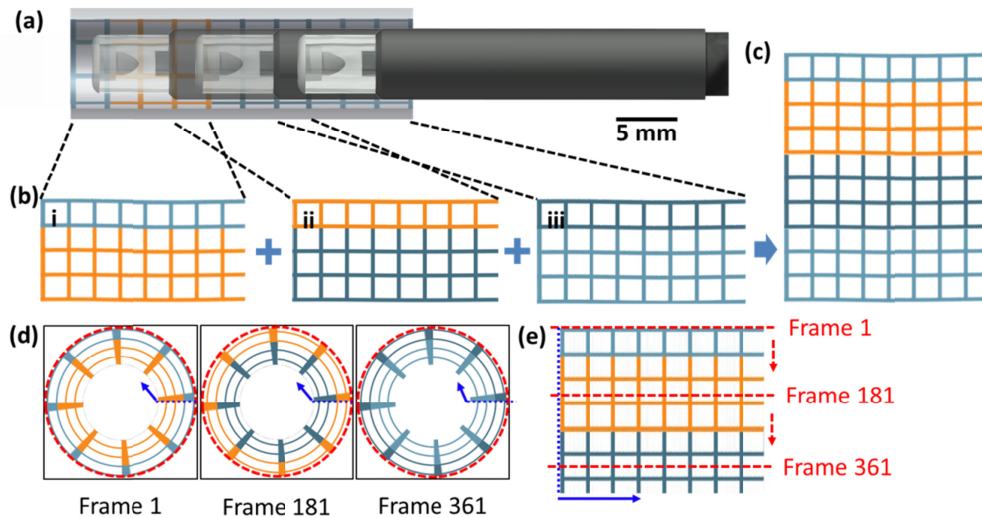
Fig. 4. Demonstration of the unwrapping and compositing processes with artificial images. (a) Schematic of panoramic image capture along the longitudinal axis. (b) Three panoramic grid images generated for testing of the algorithm. (c) Panoramic grid images unwrapped to cylinders show little distortion (d-e) Demonstration of unwrapping algorithm for video.

Image quality may become deteriorated as a result of the packaging necessary for biological applications of the endoscope. Figure 5 shows the difference between endoscope images taken in air and in the final, quartz tubing package. Packaging in quartz increased the total device diameter from 3 mm to 5 mm. Images taken in the quartz package were significantly better than in an acrylic package (not shown), but showed slightly reduced contrast compared to those in air, likely due to Fresnel reflection. The Latin script logo shown in the image has printed dimensions of 6 mm × 35 mm, while the mixed-script logo has dimensions of 3.3 × 11.7 mm.

Figure 5 demonstrates the practical application of the unwrapping and compositing algorithms from Fig. 4. The polar unwrapping and feature-based stitching of static images, demonstrated for simulated images in Fig. 3(a)-3(c), is demonstrated for practical images in Fig. 5(a)-5(c), and works well for non-continuous image capture when distortion is not a serious concern and features are shared between images. The algorithm for feature-independent stitching of the consecutive video frames from Fig. 4(d)-4(e) is applied in Fig. 5(d)-5(g).

In Fig. 5(d)-5(f) and Fig. 6(a), it can also be seen that the quality of focus of a cylindrical target varies with radial position on the imager. This is likely due to the radial dependence of the mirror's curvature and the dependence of the object distance on the ray angle from the mirror to the object cylinder. Thus the image quality was observed to depend relatively little on optomechanical assembly tolerances. When imaging a fixed-radius object cylinder, a small (< 0.5 mm) deviation in lens-mirror distance during assembly only resulted in a radial shift of the point of best focus. For this reason, it was also difficult to determine the focal distance and focal depth of the device: following assembly, cylindrical target objects at working distances of 0 to 10 mm, measured radially from the quartz tube (5.0 to 9.9 mm diameter), were focused at different regions of the image sensor.
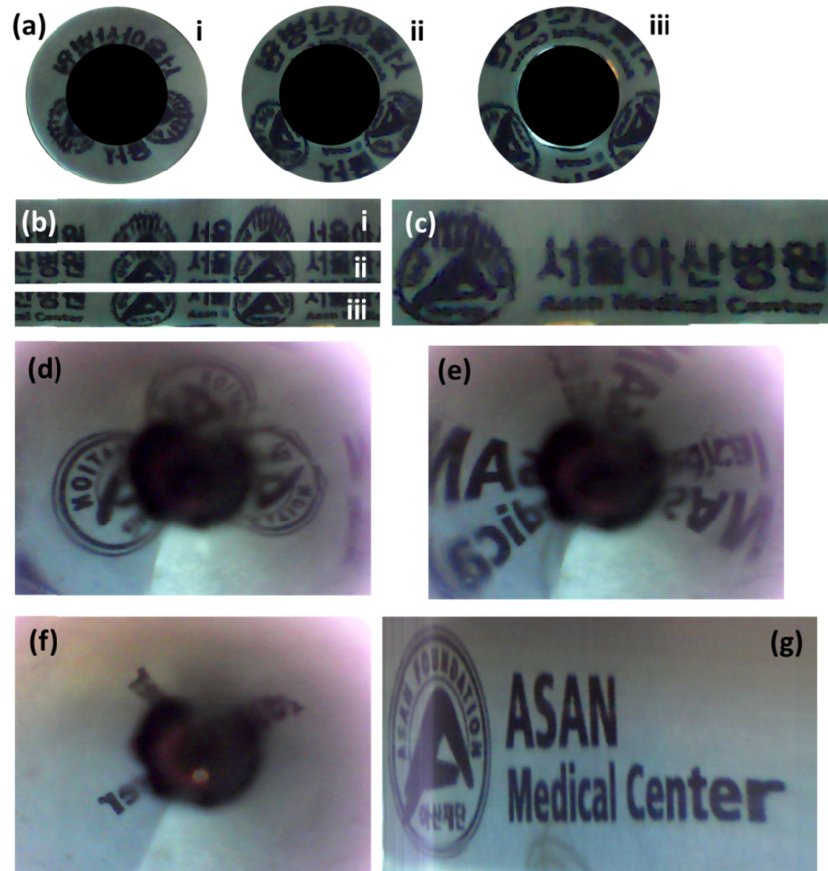
Fig. 5. Sample unwrapping and compositing of test images, comparing the endoscope packaged within and outside of a quartz tube. (a) Wrapped cylindrical logo in air, imaged at three longitudinal points. (b) Unwrapped cylindrical logo for each of the images in (a). (c) Composite image of the images in (b). (d,e,f) With the probe packaged in a quartz tube, frames taken from a video of the wrapped cylindrical logo. (g) Frames unwrapped from the video in (d,e,f) show decreased contrast due to Fresnel reflections, but reduced image distortion and higher resolution overall. The unwrapping and composting of (a-c) demonstrates the algorithm used in Fig. 3(a)-3(c), which works well for nonconsecutive images with shared features, while that of (d-g) demonstrates the algorithm of Fig. 3(e)-3(f), which applies well to video images.

Figure 6 shows the modulation transfer function of the quartz-packaged endoscope, as calculated by the slanted edge method. The contrast remains above 0.2 until 23 lp/mm, which corresponds to 600 dpi. This performance is much less than expected, and can be explained by a combination of the low resolution of the printed target, and the focal limitations of the system.
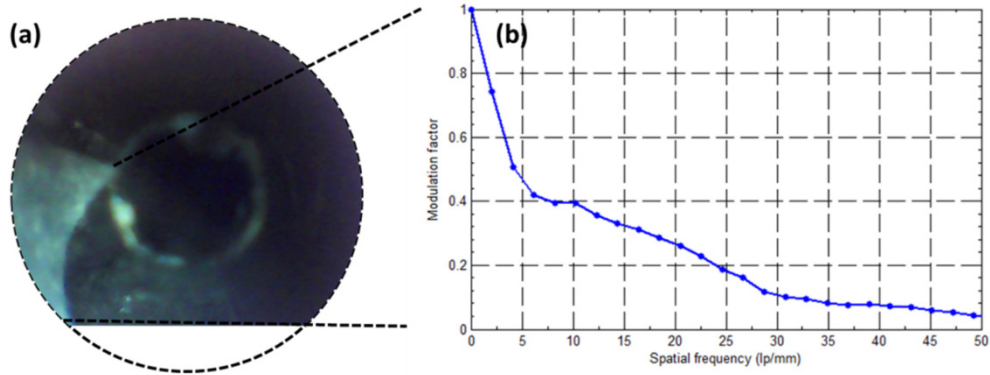
Fig. 6. Slant edge derivation of modulation transfer function. (a) Raw image. (b) MTF.

The fabricated endoscope was further tested by insertion into a pediatric vascular 3D-printed model mimicking a real congenital heart disease patient. A continuous video was captured while the probe was removed from the cardiac phantom. Following the method from Fig. 4(e) and 4(f), a circular section (red dashes) was interpolated from each frame into a cylindrical image, as shown in Fig. 7(a). The probe clearly captured diverging arteries (blue arrows) in the original video (Fig. 7(b)), as well as in the unwrapped image (Fig. 7(c)). The well-focused texture of the vascular phantom can be seen in the unwrapped image. The obtained image can be re-wrapped around a 3D model for a fly-through examination of the cardiac phantom, as shown in Fig. 7(d). This is the first realistic phantom image captured by a miniaturized catadioptric endoscope probe.
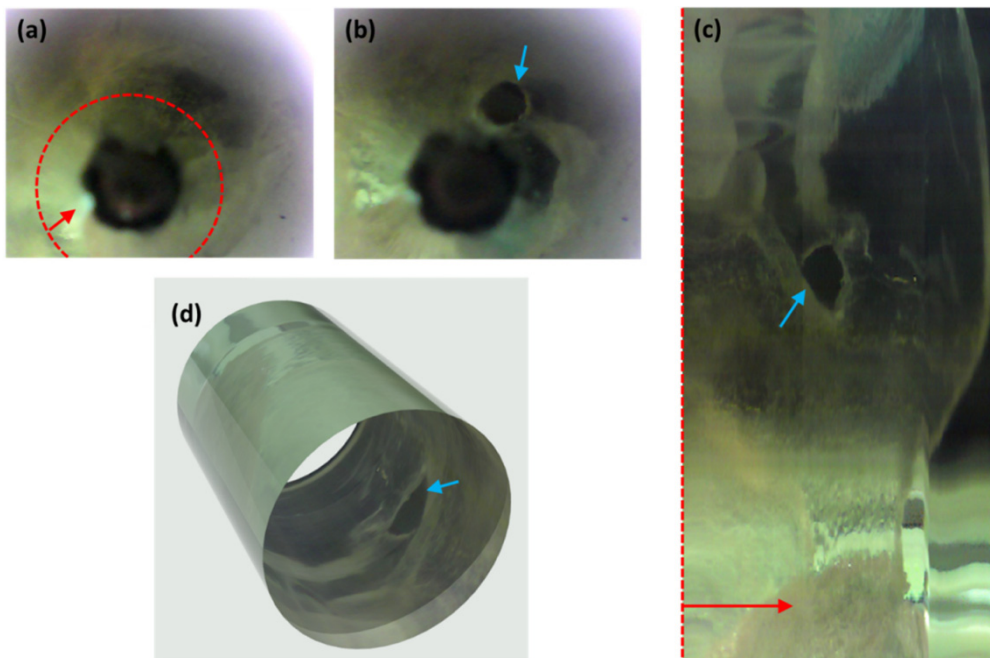

Fig. 7. Cylindrical imaging of a pediatric cardiac phantom. (a) Initial frame with overlaid extracted circular imaging region (red dash). (b) branching of artery is observed in the phantom (blue arrow). (c) The unwrapped cylindrical image, with the first frame imaging region marked (red dash). The imaging direction arrow (red) matches that in (a). (d) The image re-wrapped onto a cylinder in 3D modelling software for a fly-through examination.

4. Conclusion

We report on the realization of a miniaturized flexible catadioptric sensor capable of panoramic view and composite image generation, with applications to pediatric diagnosis and small animal model endoscopy. The device performance was evaluated theoretically and experimentally, showing efficient performance compared to previously published larger prototypes, and significant performance given the miniaturized device type. Following simulations, MTF was calculated to be above 0.2 at 25 lp/mm. Field of view was 50° by 360°, which is exceptional for a side-view device. The device prototype is demonstrated in a pediatric cardiac phantom to give acceptable images in a packaged diameter of 5 mm, and may be further miniaturized by suitable packaging. In short, this family of miniaturized single-fold catadioptric devices is expected to be highly useful for the rapid diagnosis and treatment of thin tubular biostructures.

Disclosures

The authors declare that there are no conflicts of interest related to this article.

References

1. G. L. Mariottini and D. Prattichizzo, "Image-based Visual Servoing with Central Catadioptric Cameras," Int. J. Robot. Res. **27**(1), 41–56 (2008).
2. A. Basu and D. Southwell, "Omni-directional sensors for pipe inspection," in 1995 IEEE International Conference on Systems, Man and Cybernetics. Intelligent Systems for the 21st Century (1995), Vol. 4, pp. 3107–3112 vol.4.
3. S. K. Nayar, "Omnidirectional Video Camera," in Proc. of DARPA Image Understanding Workshop (1997).
4. Y. Onoe, N. Yokoya, K. Yamazawa, and H. Takemura, "Visual surveillance and monitoring system using an omnidirectional video camera," in Proceedings. Fourteenth International Conference on Pattern Recognition (Cat. No.98EX170) (IEEE Comput. Soc, 1998), Vol. 1, pp. 588–592.
5. R. Katkam, B. Banerjee, C. Y. Huang, X. Zhu, L. Ocampo, J.-L. Kincade, and R. Liang, "Compact dual-view endoscope without field obscuration," J. Biomed. Opt. **20**(7), 076007 (2015).
6. R. C. C. Wang, M. J. Deen, D. Armstrong, and Q. Fang, "Development of a catadioptric endoscope objective with forward and side views," J. Biomed. Opt. **16**(6), 066015 (2011).
7. M.-J. Sheu, C.-W. Chiang, W.-S. Sun, J.-J. Wang, and J.-W. Pan, "Dual view capsule endoscopic lens design," Opt. Express **23**(7), 8565–8575 (2015).
8. D. Shin, M.-A. Protano, A. D. Polydorides, S. M. Dawsey, M. C. Pierce, M. K. Kim, R. A. Schwarz, T. Quang, N. Parikh, M. S. Bhutani, F. Zhang, G. Wang, L. Xue, X. Wang, H. Xu, S. Anandasabapathy, and R. R. Richards-Kortum, "Quantitative Analysis of High-Resolution Microendoscopic Images for Diagnosis of Esophageal Squamous Cell Carcinoma," Clin. Gastroenterol. Hepatol. **13**(2), 272–279 (2015).
9. P. Kim, E. Chung, H. Yamashita, K. E. Hung, A. Mizoguchi, R. Kucherlapati, D. Fukumura, R. K. Jain, and S. H. Yun, "In vivo wide-area cellular imaging by side-view endomicroscopy," Nat. Methods **7**(4), 303–305 (2010).
10. M. A. Tadayon, I. Pavlova, K. M. Martyniuk, A. Mohanty, S. P. Roberts, F. Barbosa, C. A. Denny, and M. Lipson, "Microphotonic needle for minimally invasive endoscopic imaging with sub-cellular resolution," Sci. Rep. **8**(1), 10756 (2018).
11. O. G. Opitz, H. Harada, Y. Suliman, B. Rhoades, N. E. Sharpless, R. Kent, L. Kopelovich, H. Nakagawa, and A. K. Rustgi, "A mouse model of human oral-esophageal cancer," J. Clin. Invest. **110**(6), 761–769 (2002).

12. X. Chen, Y. W. Ding, G. Yang, F. Bondoc, M. J. Lee, and C. S. Yang, "Oxidative damage in an esophageal adenocarcinoma model with rats," Carcinogenesis **21**(2), 257–263 (2000).
13. N. S. Buttar, K. K. Wang, O. Leontovich, J. Y. Westcott, R. J. Pacifico, M. A. Anderson, K. K. Krishnadath, L. S. Lutzke, and L. J. Burgart, "Chemoprevention of esophageal adenocarcinoma by COX-2 inhibitors in an animal model of Barrett's esophagus," Gastroenterology **122**(4), 1101–1112 (2002).
14. N. Hite, A. Klinger, L. Hellmers, G. A. Maresh, P. E. Miller, X. Zhang, L. Li, and D. A. Margolin, "An Optimal Orthotopic Mouse Model for Human Colorectal Cancer Primary Tumor Growth and Spontaneous Metastasis," Dis. Colon Rectum **61**(6), 698–705 (2018).
15. A. Fumagalli, S. J. E. Suijkerbuijk, H. Begthel, E. Beerling, K. C. Oost, H. J. Snippert, J. van Rheenen, and J. Drost, "A surgical orthotopic organoid transplantation approach in mice to visualize and study colorectal cancer progression," Nat. Protoc. **13**(2), 235–247 (2018).
16. I. H. Kim, "Orthotopic Implantation and Observation using Endoscope and Confocal microscope with Side-view endoscope: Usefulness as an Experimental Animal Model of Colon Cancer," Ph.D. Thesis, Kangwon National University, Korea (2014).
17. M. Pocard, H. Tsukui, R. J. Salmon, B. Dutrillaux, and M. F. Poupon, "Efficiency of orthotopic xenograft models for human colon cancers," In Vivo **10**(5), 463–469 (1996).
18. E. Zigmond, Z. Halpern, E. Elinav, E. Brazowski, S. Jung, and C. Varol, "Utilization of Murine Colonoscopy for Orthotopic Implantation of Colorectal Cancer," PLoS One **6**(12), e28858 (2011).
19. A. Klimas and E. Entcheva, "Toward microendoscopy-inspired cardiac optogenetics in vivo: technical overview and perspective," J. Biomed. Opt. **19**(8), 080701 (2014).
20. R. P. J. Barretto, T. H. Ko, J. C. Jung, T. J. Wang, G. Capps, A. C. Waters, Y. Ziv, A. Attardo, L. Recht, and M. J. Schnitzer, "Time-lapse imaging of disease progression in deep brain areas using fluorescence microendoscopy," Nat. Med. **17**(2), 223–228 (2011).
21. T. F. Vandamme, "Use of rodents as models of human diseases," J. Pharm. Bioallied Sci. **6**(1), 2–9 (2014).
22. M. R. L. Stone, M. S. Butler, W. Phetsang, M. A. Cooper, and M. A. T. Blaskovich, "Fluorescent Antibiotics: New Research Tools to Fight Antibiotic Resistance," Trends Biotechnol. **36**(5), 523–536 (2018).
23. M. Pellisé, G. Fernández-Esparrach, A. Cárdenas, O. Sendino, E. Ricart, E. Vaquero, A. Z. Gimeno-García, C. R. de Miguel, M. Zabalza, A. Ginès, J. M. Piqué, J. Llach, and A. Castells, "Impact of Wide-Angle, High-Definition Endoscopy in the Diagnosis of Colorectal Neoplasia: A Randomized Controlled Trial," Gastroenterology **135**(4), 1062–1068 (2008).
24. N. Barker, R. A. Ridgway, J. H. van Es, M. van de Wetering, H. Begthel, M. van den Born, E. Danenberg, A. R. Clarke, O. J. Sansom, and H. Clevers, "Crypt stem cells as the cells-of-origin of intestinal cancer," Nature **457**(7229), 608–611 (2009).
25. J. K. Kim, W. M. Lee, P. Kim, M. Choi, K. Jung, S. Kim, and S. H. Yun, "Fabrication and operation of GRIN probes for in vivo fluorescence cellular imaging of internal organs in small animals," Nat. Protoc. **7**(8), 1456–1469 (2012).
26. Q. Liu, J. Bai, and Y. Luo, "Design of high resolution panoramic endoscope imaging system based on freeform surface," J. Phys. Conf. Ser. **680**, 012011 (2016).
27. Z.-R. Yu, C.-F. Ho, A. Liu, T.-W. Lee, W.-L. Lin, and W.-Y. Hsu, "Design and development of bi-directional viewer," in R. B. Johnson, V. N. Mahajan, and S. Thibault, eds. (2012), p. 848613.
28. M. Ou-Yang and W.-D. Jeng, "Design and analysis of radial imaging capsule endoscope (RICE) system," Opt. Express **19**(5), 4369–4383 (2011).
29. S.-S. Lin and R. Bajcsy, "Single-viewpoint, catadioptric cone mirror omnidirectional imaging theory and analysis," J. Opt. Soc. Am. A **23**(12), 2997–3015 (2006).
30. S. Baker and S. K. Nayar, "A Theory of Single-Viewpoint Catadioptric Image Formation," Int. J. Comput. Vis. **35**(2), 175–196 (1999).
31. S. Sahli, R. Wang, A. Murthy, D. Arnstrong, M. J. Deen, and Q. Fang, "A 360 degree side view endoscope for lower gi tract mapping," Phys. Can. **71**, 18–20 (2015).
32. J. C. Aparicio Fernandes and J. A. B. Campos Neves, "Using Conical and Spherical Mirrors with Conventional Cameras for 360°; Panorama Views in a Single Image," in 2006 IEEE International Conference on Mechatronics (IEEE, 2006), pp. 157–160.
33. D. Do, H. Yoo, and D.-G. Gweon, "Fiber-optic raster scanning two-photon endomicroscope using a tubular piezoelectric actuator," J. Biomed. Opt. **19**, 066010 (2014).
34. C. Mitja, J. Escofet, A. Tachó, and R. Revuelta, "Slanted Edge MTF," https://imagej.nih.gov/ij/plugins/se-mtf/index.html.
35. M. Brown and D. G. Lowe, "Automatic Panoramic Image Stitching using Invariant Features," Int. J. Comput. Vis. **74**(1), 59–73 (2007).